nature nanotechnology

Article

https://doi.org/10.1038/s41565-023-01456-6

Step engineering for nucleation and domain orientation control in WSe_2 epitaxy on *c*-plane sapphire

Received: 18 October 2022

Accepted: 13 June 2023

Haoyue Zhu[1,13], Nadire Nayir[1,2,3,13], Tanushree H. Choudhury[1,4,13], Anushka Bansal[5], Benjamin Huet[1], Kunyan Zhang[6], Alexander A. Puretzky[7], Saiphaneendra Bachu[5], Krystal York[8], Thomas V. Mc Knight[5], Nicholas Trainor[5], Aaryan Oberoi[9], Ke Wang[10], Saptarshi Das[1,9], Robert A. Makin[8], Steven M. Durbin[8], Shengxi Huang[6,11], Nasim Alem[1,5], Vincent H. Crespi[1,12], Adri C. T. van Duin[1,3] & Joan M. Redwing[1,5]

Epitaxial growth of two-dimensional transition metal dichalcogenides on sapphire has emerged as a promising route to wafer-scale single-crystal films. Steps on the sapphire act as sites for transition metal dichalcogenide nucleation and can impart a preferred domain orientation, resulting in a substantial reduction in mirror twins. Here we demonstrate control of both the nucleation site and unidirectional growth direction of WSe_2 on *c*-plane sapphire by metal–organic chemical vapour deposition. The unidirectional orientation is found to be intimately tied to growth conditions via changes in the sapphire surface chemistry that control the step edge location of WSe_2 nucleation, imparting either a 0° or 60° orientation relative to the underlying sapphire lattice. The results provide insight into the role of surface chemistry on transition metal dichalcogenide nucleation and domain alignment and demonstrate the ability to engineer domain orientation over wafer-scale substrates.

Two-dimensional (2D) transition metal dichalcogenides (TMDs) with desired properties are promising candidates for applications such as three-dimensional integrated devices on Si complementary metal–oxide–semiconductors, sensors and optoelectronics[1–4]. In addition to the intensively studied MoS_2, monolayer WSe_2—a direct bandgap semiconductor with an optical gap of ~1.65 eV—also exhibits attractive properties[5,6]. WSe_2 is distinguished from other TMDs by its enhanced spin–orbit coupling and large splitting of the valence band maximum (0.46 eV for WSe_2 compared with 0.15 eV for MoS_2), making it a promising material for spintronics[7,8]. The ambipolar characteristics of WSe_2 also enable p-type behaviour, rather than the commonly observed n-type doping in WS_2 and MoS_2[9–12].

Owing to the small size of mechanically exfoliated flakes from bulk crystals, research has focused on epitaxial growth of TMDs as a pathway

---

[1] 2D Crystal Consortium Materials Innovation Platform, Materials Research Institute, The Pennsylvania State University, University Park, PA, USA. [2] Department of Physics, Karamanoglu Mehmetbey University, Karaman, Turkey. [3] Department of Mechanical Engineering, The Pennsylvania State University, University Park, PA, USA. [4] Department of Metallurgical Engineering and Materials Science, Indian Institute of Technology Bombay, Mumbai, India. [5] Department of Materials Science and Engineering, The Pennsylvania State University, University Park, PA, USA. [6] Department of Electrical Engineering, The Pennsylvania State University, University Park, PA, USA. [7] Center for Nanophase Materials Sciences, Oak Ridge National Laboratory, Oak Ridge, TN, USA. [8] Department of Electrical Engineering, Western Michigan University, Kalamazoo, MI, USA. [9] Department of Engineering Science and Mechanics, The Pennsylvania State University, University Park, PA, USA. [10] Materials Research Institute, The Pennsylvania State University, University Park, PA, USA. [11] Department of Electrical and Computer Engineering, Rice University, Houston, TX, USA. [12] Department of Physics, The Pennsylvania State University, University Park, PA, USA. [13] These authors contributed equally: Haoyue Zhu, Nadire Nayir, Tanushree H. Choudhury. e-mail: jmr31@psu.edu

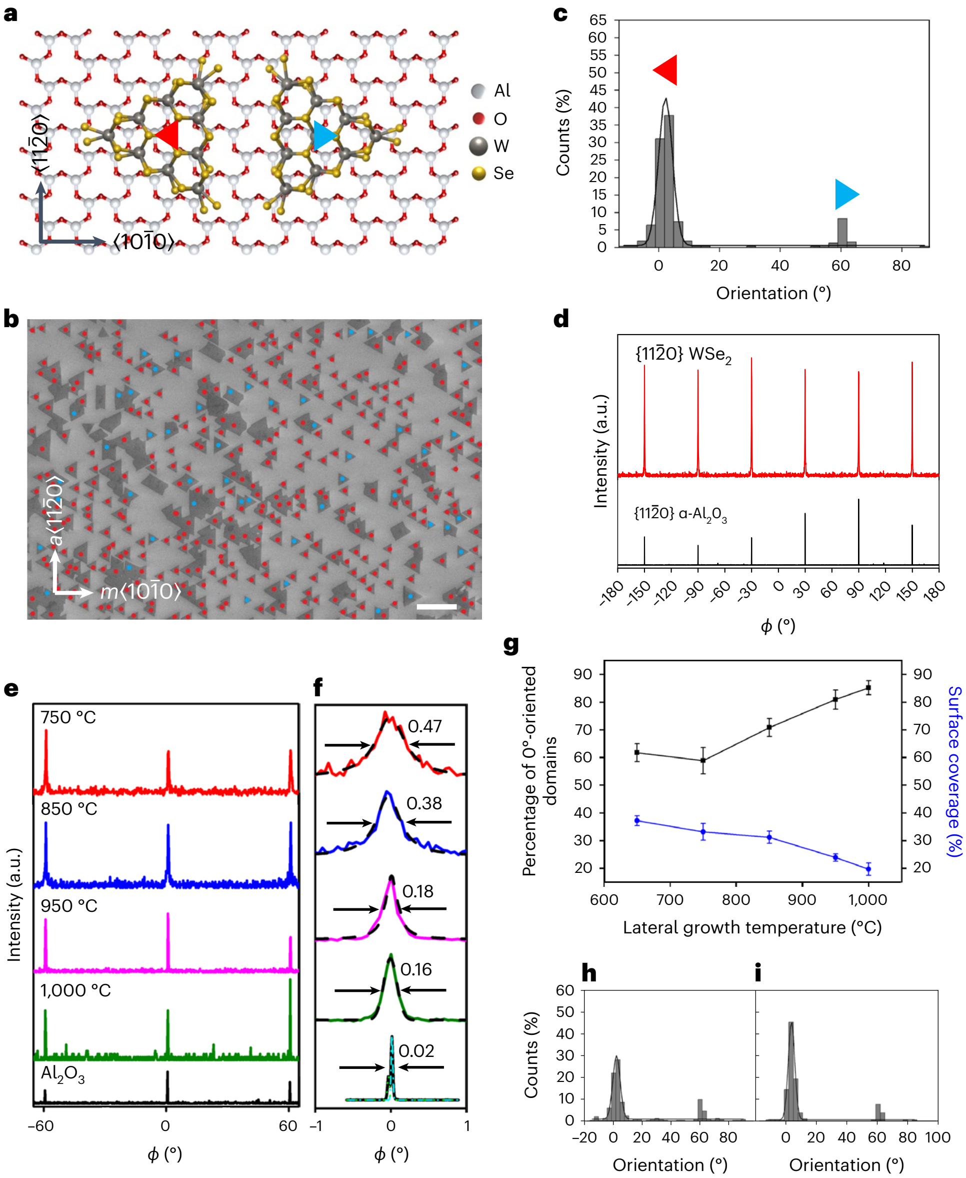

Fig. 1 | Preferred orientation of WSe$_2$ domains. a,**b**, Schematic illustration (**a**) and scanning electron microscopy image (**b**) of WSe$_2$ domains showing preferred orientations of 0°- (red) and 60°- (blue) oriented WSe$_2$. Scale bar in **b**, 1 µm. **c**, Orientation histogram of the isolated WSe$_2$ domains in **b**. **d**, In-plane X-ray diffraction (XRD) azimuthal angle (ϕ) scans of {11$\bar{2}$0} planes of WSe$_2$ and α-Al$_2$O$_3$ confirming the six-fold [11$\bar{2}$0] WSe$_{2(0001)}$//[11$\bar{2}$0] α-Al$_2$O$_{3(0001)}$ epitaxial relationship where // indicates parallel planes. a.u., arbitrary units. **e**, In-plane XRD ϕ scans of {10$\bar{1}$0} planes of WSe$_2$ as a function of lateral growth temperature. **f**, The full-width and half-maximum (FWHM) of the WSe$_2$ ϕ scan peak decreases with increasing temperature, indicating a reduction in in-plane rotational misorientation. **g**–**i**, Percentage of 0°-oriented WSe$_2$ domains and surface coverage as a function of growth temperature obtained from atomic force microscopy (AFM) images (**g**) and orientation histograms at growth temperatures of 650 °C (**h**) and 950 °C (**i**) (see also Supplementary Fig. 5). Data are presented as mean ± s.d. obtained on three different areas of samples.

to wafer-scale single-crystal monolayers and few-layer films[13,14]. *C*-plane sapphire ((0001) α-Al$_2$O$_3$) has emerged as a promising substrate for epitaxy due to its crystallographic compatibility, chemical and thermal stability under typical growth environments and commercial availability in wafer diameters up to 200 mm. Epitaxial growth of WSe$_2$ on *c*-plane α-Al$_2$O$_3$ has been demonstrated[15–17], with growth on a 1 × 1 Al-terminated (0001) sapphire surface exhibiting commensurability via a three-on-two superstructure (*a* lattice parameters: a_{WSe2} = 3.30 Å and $a_{\alpha\text{-Al2O3}}$ = 4.76 Å) where the WSe$_2$ was aligned in the same crystallographic direction as the α-Al$_2$O$_3$ (Fig. 1a and Supplementary Fig. 1)[17]. The non-centrosymmetric D_{3h} lattice of TMDs leads to the equivalency of antiparallel domains with lattice rotation angles of 0° and 60° (Fig. 1a) or ±30° relative to the ⟨11$\bar{2}$0⟩ axis[18]. The merging of domains with 60° in-plane rotation leads to the formation of inversion domain boundaries (IDBs), also referred to as mirror twin grain boundaries[19,20]. IDBs have been demonstrated to exhibit metallic character and can act as conducting channels within the semiconducting monolayer that negatively impact both electrical and optical properties[21–23].

Steps on the surface of the *c*-plane sapphire play an important role in TMD nucleation and orientation. On-axis *c*-plane sapphire substrates typically have a miscut angle of ~0.2° towards the *m* axis (⟨10$\bar{1}$0⟩), which produces steps that are aligned roughly parallel to the *a* axis (⟨11$\bar{2}$0⟩) (Supplementary Fig. 2). Chen et al. demonstrated that the steps act as preferred sites for WSe$_2$ nucleation and impart directionality to the growing domains[24]. Similar unidirectional domains have been reported for epitaxial growth of WS$_2$ (ref. 25) and MoS$_2$ (ref. 26) on *c*-plane

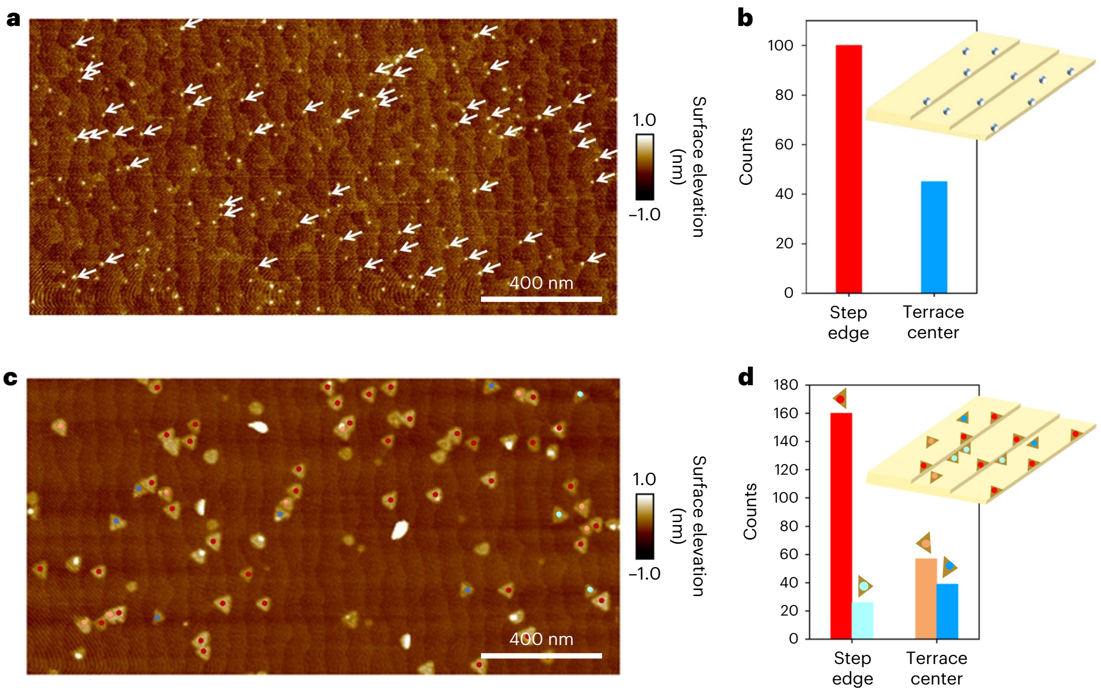

Fig. 2 | Domain nucleation at step edges. a, AFM image showing WSe_x nuclei on the sapphire substrate after nucleation and ripening. The white arrows highlight the nuclei localized at the step edges. **b**, Position distribution and schematic (inset) of nuclei at step edges and terrace centres. **c**, AFM image of WSe_2 domains after 5 min of lateral growth. The dots on the domains are colour coded according to their location and orientation. **d**, Position distribution and schematic (inset) of domains.

sapphire miscut ~0.2° towards the *m* and *a* axes, respectively. However, the presence of steps alone is not sufficient to achieve epitaxy and unidirectional domains, as previous work has demonstrated the need for specific growth conditions such as the presence of H_2 (ref. 27), a high sulfur flux[28] or metal seeding of the surface[29]. Consequently, both the presence of steps and the growth chemistry play a role in TMD nucleation and alignment.

In this study we demonstrate that the nucleation of WSe_2 on step edges can be switched from the top to the bottom edge of the step by varying growth conditions, resulting in a change in the preferred domain orientation from 0° to 60°, respectively. Our combined experimental and theoretical results provide insight into the role of surface step structure and chemistry on TMD nucleation and domain alignment, which can be exploited to reproducibly achieve wafer-scale single-crystal monolayers.

WSe_2 monolayer films were grown by metal–organic chemical vapour deposition (MOCVD) on 50-millimeter-diameter *c*-plane sapphire substrates using a modified three-step process (nucleation, ripening, lateral growth)[15] with $W(CO)_6$ and H_2Se as precursors in a H_2 carrier gas (Methods and Supplementary Fig. 3). At a reactor pressure of 200 torr and with 10 min lateral growth time, isolated WSe_2 domains were present on the substrate, which enabled a determination of their orientation relative to the underlying sapphire (Fig. 1b,c). The WSe_2 domains pointed along the $[10\bar{1}0]$ and $[\bar{1}0\bar{1}0]$ axes, which were designated the 0° and 60° domains, respectively (Fig. 1a). Statistical analysis indicates that ~87% of the domains exhibited a 0° orientation, while the remainder were 60° (Fig. 1c and Supplementary Fig. 4). In-plane XRD ϕ scans of the $\{11\bar{2}0\}$ planes of WSe_2 and α-Al_2O_3 showed six-fold rotational symmetry and demonstrate that the WSe_2 grew epitaxially on the substrate with the epitaxial relationship of $[11\bar{2}0]WSe_{2(0001)}$//$[11\bar{2}0]\alpha$-$Al_2O_{3(0001)}$ (Fig. 1d).

The effect of growth temperature on WSe_2 domain orientation was probed by varying the lateral growth temperature from 650 °C to 1,000 °C (Methods and Supplementary Fig. 3). Again, in-plane XRD ϕ scans showed an epitaxial relationship of $[11\bar{2}0]WSe_{2(0001)}$//$[11\bar{2}0]$ α-$Al_2O_{3(0001)}$ for growth temperatures from 750 °C to 1,000 °C (Fig. 1e). The FWHM of the ϕ scan peak of WSe_2, which is a measure of the in-plane rotational misorientation of domains[30], decreased from 0.47° at 750 °C to 0.16° at 1,000 °C indicating an improvement in the epitaxial registry at higher growth temperatures (Fig. 1f). The percentage of 0°-oriented domains increased from ~60% for the WSe_2 sample grown at 650–750 °C to ~85% for the WSe_2 grown at 1,000 °C (Fig. 1g–i and Supplementary Fig. 5).

Mechanism of domain orientation

To investigate the origin of the preferred orientation, WSe_2 growth was terminated after the nucleation and ripening steps. A substantial fraction of the WSe_2 nuclei (white dots) were localized at the top edge of the steps (Fig. 2a,b). After lateral growth of 5 min, the nuclei grew into triangular domains (Fig. 2c). The domains near the terrace centres showed both the 0° (orange) and 60° (blue) orientations, present in similar fractions (Fig. 2d). However, the domains that nucleated at the top edge of the step (red) were much more frequently observed than those that initiated at the bottom step edge (light blue).

The role of steps as nucleation sites is well established in traditional epitaxy and has been reported previously for TMD growth on *c*-plane sapphire[24,27]. The bottom edge of the step is typically the thermodynamically preferred site for nucleation due to the preponderance of dangling bonds. Our observations, however, show that the nuclei are localized at the top edge of the steps with their zigzag edge roughly aligned to the step edge, and grow across the terrace, rather than over the step edge, giving rise to the observed 0° orientation.

The WSe_2 orientation is not solely determined by the step direction, however, which can vary by several degrees from substrate to substrate (Fig. 3a,b). The WSe_2 domains do not align with the steps, they instead retain the $[11\bar{2}0]WSe_{2(0001)}$//$[11\bar{2}0]\alpha$-$Al_2O_{3(0001)}$ epitaxial

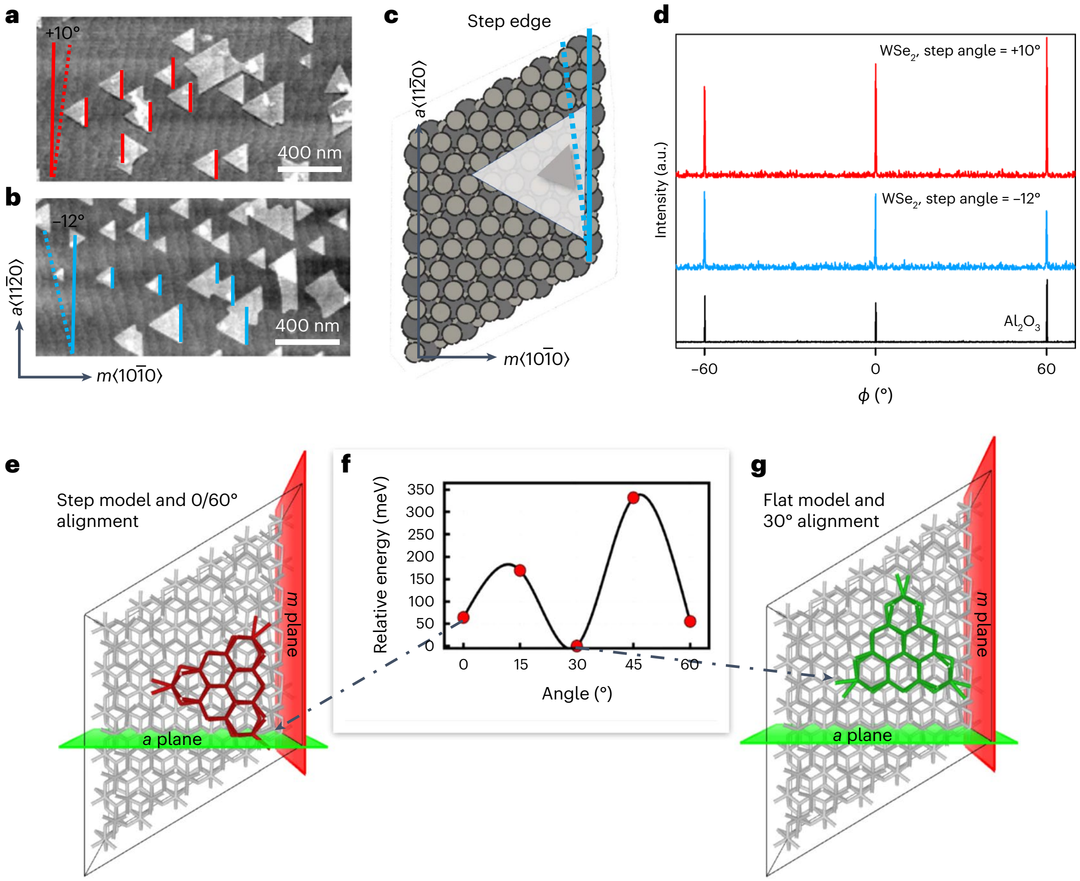

Fig. 3 | Competition between the step edge and underlying sapphire symmetry. a,**b**, Two samples where the steps are oriented at +10° (**a**) and −12° (**b**) relative to the *a* axis of the sapphire, yet the zigzag edges of the WSe_2 domains remain parallel to the *a* ⟨11$\bar{2}$0⟩ axis. **c**, Schematic illustration of WSe_2 domain aligned to underlying lattice (solid line) rather than step edge (dashed line). **d**, In-plane XRD ϕ scans of {11$\bar{2}$0} planes confirming that the WSe_2 remains epitaxially aligned with the Al_2O_3. **e**–**g**, Schematic illustrations of WSe_2 alignment on sapphire in the presence (**e**) and absence (**g**) of step edge compared to the relative energy of WSe_2 domain orientations (red circles) (**f**) on flat *c*-plane sapphire as a function of orientation angle. The black curve in **f** is a guide for the eye.

relationship (Fig. 3c,d). Similar results have been reported for MoS_2 epitaxy on *c*-plane sapphire[31]. At the early stage of growth, when WSe_2 nuclei have not yet obtained their equilibrium zigzag structure, the nuclei have slanted edges with kinks that interact strongly with the step edges (Supplementary Information and Supplementary Fig. 6). The slanted edges disappear quickly during kink flow growth of the edge, leading to completion of the linear zigzag edge that is aligned parallel to the A ⟨11$\bar{2}$0⟩ axis, rather than the step edge. Thus, while the steps act as sites for nucleation and impart directionality, the WSe_2 domains remain oriented to the underlying *c*-plane sapphire lattice regardless of the exact step angle. It should be noted that WS_2 domains grown by MOCVD using $W(CO)_6$ and H_2S on similar *c*-plane sapphire substrates were previously reported to be more strongly influenced by the structure and direction of the step edges[25]. This is probably due to differences in the growth chemistry of sulfur versus selenium TMDs.

Density functional theory (DFT) calculations were carried out to explore the epitaxial relationship between WSe_2 and flat *c*-plane sapphire to assess the role of the steps. Thermal annealing of *c*-plane sapphire in H_2 at high temperatures (~900 °C) is known to alter the sapphire surface, resulting in a loss of −OH groups and leaving an Al-terminated surface[32]. Given the high-temperature (850–1,000 °C), H_2-rich growth environment, the *c*-plane sapphire surface is assumed to be 1 × 1 Al-terminated, as in previous reports[14]. Direct epitaxy of WSe_2 on Al-terminated sapphire would destroy the van der Waals nature of the interface (Supplementary Fig. 8a). Therefore, the Al-terminated surface is assumed to react readily with H_2Se, which is present in excess in the growth ambient, resulting in a Se-passivated surface (Supplementary Fig. 8b). The WSe_2 then interacts with the Se-passivated sapphire surface via quasi-van der Waals epitaxy, which is consistent with the interface chemistry and structure as assessed by high-angle annular dark-field scanning transmission electron microscopy (HAADF STEM) (Supplementary Fig. 8c–e) and energy-dispersive spectroscopy (Supplementary Fig. 8f).

The relative total energies of different orientations of WSe_2 on Se-passivated *c*-plane sapphire were then computed by rotating a WSe_2 cluster with a dimension of 13.16 Å with respect to the [10$\bar{1}$0] direction of sapphire (Supplementary Fig. 9). On flat Se-passivated sapphire, the 30° orientation of WSe_2 was found to be a more stable configuration (Fig. 3f). However, as shown in Figs. 1–3 and other reports[15,17], the 0°/60° orientations are observed experimentally. This suggests that the presence of step edges along the A ⟨11$\bar{2}$0⟩ axis, which act as sites for WSe_2 nucleation, induced the 0/60° alignment (Fig. 3e,f), instead of the predicted 30° alignment (Fig. 3f,g). The Se termination led to the two local minima (0°/60° and 30°) with a slight deviation (Fig. 3f and Supplementary Fig. 9), in accordance with previous work[33]. The presence of step edges can enable the domains to overcome the small energy differences between two local minima and favour the second energetically stable point; that is, the 0°/60° configuration. Interactions between a Se-terminated substrate and WSe_2 are also considerably weaker than those with Al-terminated sapphire; neighbouring domains

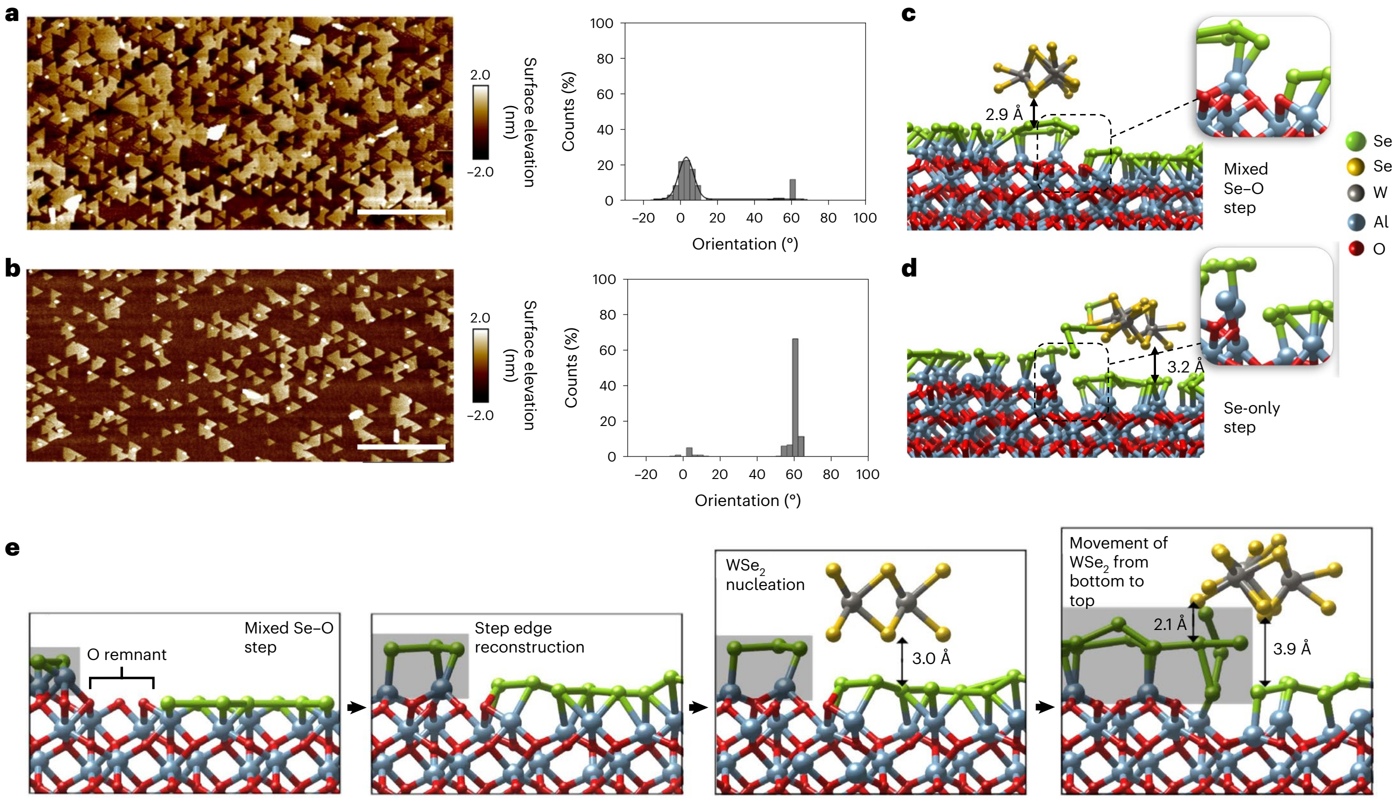

Fig. 4 | Domain orientation and step edge termination. a,**b**, AFM images (left) and histograms (right) of WSe$_2$ domains grown on *c*-plane sapphire at 200 torr (**a**) and 700 torr (**b**), showing the preferred orientations of 0° and 60°, respectively. Scale bars, 1 µm. **c**,**d**, Optimized configurations of a mixed Se–O (**c**) sapphire step with magnified view (right) showing oxygen atoms on the bottom terrace next to the step edge and Se-only (**d**) sapphire step with magnified view (right) showing no oxygen atoms at bottom of step. Yellow indicates Se atoms in WSe$_2$ while green indicates Se atoms in passivation layer on sapphire. **e**, Step edge reconstruction of mixed Se–O sapphire step. During the relaxation, the existence of O remnants (left) leads to the step edge reconstruction (middle left) (highlighted with a grey shading), then the movement of WSe$_2$ from the bottom (middle right) to the top terrace (right) as also shown in Supplementary Fig. 11 and Supplementary Videos 1–4.

with dangling bonds can consequently induce the 0°/60° alignment of domains on terraces, as reported previously[28,33]. The presence of *a* ⟨11$\bar{2}$0⟩ steps reduces symmetry by external perturbation (for example, high adsorption sites on step edges) and removes the degeneracy in the formation energy of WSe$_2$ on sapphire (Fig. 3f); in other words, the 30° option disappears at the step edges, stabilizing the 0° (or 60°) alignment (Fig. 3e).

To further investigate the effect of growth conditions on WSe$_2$ domain orientation, additional growth experiments were carried out, in which the reactor pressure was increased from 200 torr to 700 torr, with all other conditions kept constant, to increase the partial pressure of both H_2 and H_2Se within the growth environment. As previously discussed, at 200 torr, the majority of the WSe$_2$ domains exhibited the 0° orientation (Fig. 4a), however, at 700 torr, the predominant domain direction switched to 60° (Fig. 4b). The 60° orientation observed at 700 torr indicated that the WSe$_2$ domains were now nucleating at the bottom edge of the steps, similar to previous reports for step-directed TMD growth[24,27].

DFT calculations were used to identify the thermodynamically preferred site for WSe$_2$ nucleation on the steps for comparison with the experimental results (Supplementary Fig. 10–15). The existence of an oxygen remnant on the bottom terrace next to the step edge due to incomplete removal of –OH from the sapphire surface led to WSe$_2$ growth on the top step edge, rather than the bottom (Fig. 4c–e and Supplementary Figs. 11–13). WSe$_2$ that nucleated at the top edge remained there (Supplementary Figs. 10, 12–15 and Supplementary Videos 2 and 6), whereas WSe$_2$ that initially nucleated at the bottom edge moved from the bottom to the top (Supplementary Figs. 10–15 and Supplementary Videos 1 and 5). However, for sapphire that was fully Al-terminated and passivated with Se with no O-remnant (Fig. 4d, Supplementary Figs. 14–15 and Supplementary Videos 3, 4, 7, 8), WSe$_2$ remained on the bottom of the step edge (Supplementary Fig. 14f) during relaxation, which is thermodynamically more stable than the top edge (Supplementary Fig. 14e) with an energy difference of 0.13 eV that is consistent with the result obtained at 700 torr (Fig. 4b).

DFT calculations revealed that, in the presence of steps, the extent of Al termination of the sapphire surface will be dependent on the growth conditions (Supplementary Figs. 16 and 17). As the sapphire substrate with –OH termination is heated in hydrogen, the surface releases H_2O, but this does not occur in a uniform manner. Oxygen dissociation from the top terrace is energetically more favourable (1.24 eV) than that from the middle (1.28 eV) and bottom terraces (1.73 eV) (Supplementary Fig. 17). The H_2O loss occurs at the top of the steps and the terrace regions first, and the bottom of the steps last (Supplementary Fig. 16). At lower reactor pressures, the chemical potential of hydrogen is reduced, and consequently O remnants can still be present at the bottom of the steps. In this case, it is thermodynamically more likely for the WSe$_2$ to nucleate at the top step edge, as observed experimentally at 200 torr (Fig. 4a). The results demonstrate that the preferential alignment of WSe$_2$ domains is dependent not only on the presence of steps, but also on the surface termination of the sapphire substrate and the structure and chemistry of the step edges (Supplementary Figs. 10–17).

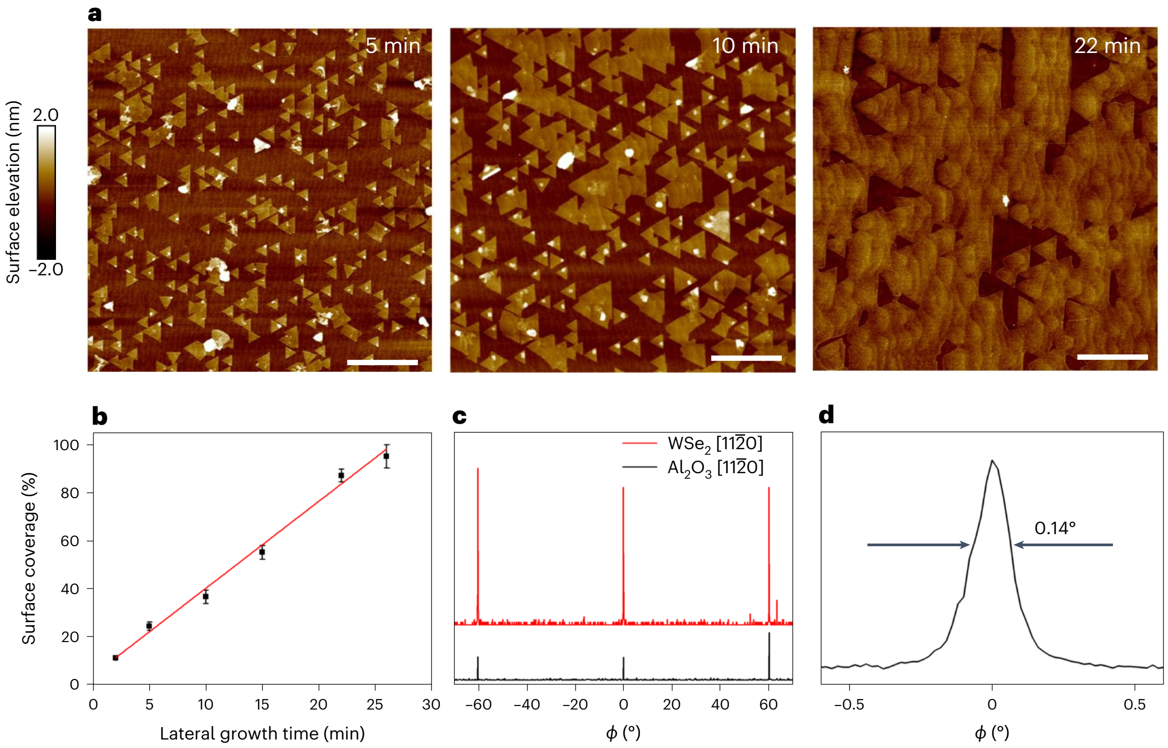

Fig. 5 | Coalescence of unidirectional WSe$_2$ domains. a,**b**, AFM images (**a**) and surface coverage (**b**) of WSe$_2$ domains as a function of lateral growth time, showing the coalescence of domains. Scale bars, 1 µm. Data are presented as mean ± s.d. obtained on five different areas of samples. Red line is a linear fit. **c**, In-plane XRD ϕ scans showing the alignment of [11$\bar{2}$0] planes of WSe$_2$ and Al$_2$O$_3$. **d**, FWHM of ϕ scan peak of WSe$_2$.

Properties of coalesced WSe$_2$ monolayers

The impact of unidirectional alignment on the properties of coalesced WSe$_2$ monolayers was assessed for films grown at a reactor pressure of 200 torr and a lateral growth temperature of 1,000 °C, which provided the highest percentage of 0°-oriented domains. The triangular WSe$_2$ domains grew laterally and began to merge with increasing growth time (Fig. 5a,b and Supplementary Figs. 18 and 19). The step width and waviness increased on the WSe$_2$ domains, compared with the underlying sapphire, probably due to further changes in the sapphire during WSe$_2$ growth. In-plane XRD of this sample confirmed that it had retained the [11$\bar{2}$0]WSe$_{2(0001)}$//[11$\bar{2}$0]α-Al$_2$O$_{3(0001)}$ epitaxial alignment (Fig. 5c) and the FWHM of the ϕ scan peak of WSe$_2$ had further narrowed to 0.14° (Fig. 5d).

Raman spectroscopy and photoluminescence measurements were carried out at room temperature on a fully coalesced WSe$_2$ monolayer that was removed from the sapphire and transferred to a SiO$_2$/Si substrate (Methods and Supplementary Fig. 20a–d). The room-temperature Raman spectrum (Supplementary Fig. 20e) shows the characteristic E^1_{2g}, A_{1g} and 2*LA* modes associated with single-layer 2H-WSe$_2$. The room-temperature photoluminescence spectrum (Supplementary Fig. 20f) shows a strong peak that can be deconvoluted into a neutral exciton peak and a negatively charged exciton (trion) peak located at ~1.68 eV and ~1.65 eV, respectively. There is negligible change in the positions of Raman and photoluminescence peaks and the FWHM as a function of position across the transferred WSe$_2$ (Supplementary Fig. 20g,h), indicating uniform properties across the wafer-scale film. Field effect transistors (FETs) were fabricated by transferring monolayer WSe$_2$ from the sapphire growth substrate to backgated test structures that incorporated a 25 nm Al$_2$O$_3$ global backgate dielectric and Pd for the source and drain contacts (Methods and Supplementary Fig. 21). Typical p-type transport was observed in the monolayer WSe$_2$ FETs with reduced device-to-device variation, low OFF currents in the range of ~10 pA, an average subthreshold slope of ~980 mV dec^{-1} and ON currents for channel length (L_{ch}) = 200 nm of ~900 nA µm^{-1}. The average field effect mobility (μ_{FE}) extracted from the transfer characteristics is ~0.4 cm^2 V^{-1} s^{-1} (Supplementary Fig. 21d). Further improvements in device performance are anticipated via the use of van der Waals and/or phase-engineered contacts[34,35] to reduce process-induced damage[36,37]. This is particularly important for monolayer WSe$_2$, which is more susceptible to degradation in ambient air and during processing than sulfide-based TMDs.

Second-harmonic generation (SHG) and dark-field transmission electron microscopy (DFTEM) were used to assess the microstructure and orientation of the coalesced WSe$_2$ monolayers. The SHG map (Fig. 6a) reveals ~2–4-µm-sized monolayer regions decorated with bilayers in 3R (red spots) and 2H (blue spots) stacking configurations, which typically are ≤1 µm in size. Polarization-resolved SHG measurements confirmed that the monolayer regions had the same crystal orientation (Methods and Supplementary Figs. 22 and 23). A composite DFTEM image (Fig. 6b), formed by stitching a 5 × 5 array of individual DFTEM images[25,38,39] (Methods and Supplementary Fig. 24), revealed the presence of triangular 60°-oriented domains outlined by trapezoidal holes (yellow circles). The holes were IDBs that were preferentially etched during the transfer process (Supplementary Fig. 24b–d). The 60° domains accounted for <10% of the 25 µm^2 viewing area (Fig. 6b), similar to the areal coverage of 60° domains measured by AFM before coalescence (Fig. 1g). Bilayer islands (bright triangles) and voids (small dark triangles) were also present, probably due to incomplete film coalescence.

The high optical quality of the WSe$_2$ was confirmed by variable-temperature photoluminescence spectroscopy. WSe$_2$ transferred onto SiO$_2$/Si exhibited two peaks in the photoluminescence spectrum at 77 K under 532 nm excitation (Supplementary Fig. 25). The photoluminescence emission at 1.730 eV was identified as the A exciton, while the

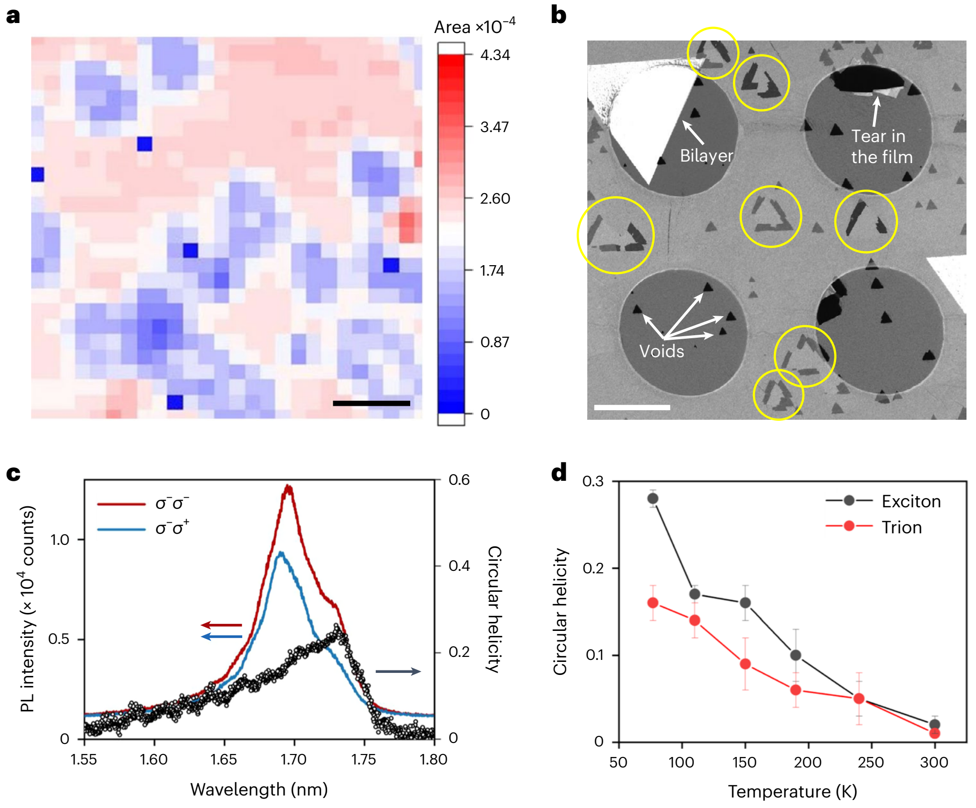

Fig. 6 | Properties of coalesced WSe_2 monolayers. a, SHG intensity map of WSe_2 on *c*-plane sapphire. Scale bar, 1 µm. **b**, Composite DFTEM map of WSe_2 transferred on a TEM grid. Scale bar, 1 µm. Inversion domains are indicated with yellow circles. **c**, Polarization-resolved photoluminescence (PL) spectra and circular helicity of transferred WSe_2 at 77 K. The incident laser was left-handed circularly polarized, and both left-handed and right-handed circular polarizations were collected, denoted $\sigma_-\sigma_-$ and $\sigma_-\sigma_+$. **d**, Circular helicities at the energies of the exciton and trion as a function of temperature. The error bars represent 1 s.d. of the fitting parameters from the least-squares fit.

peak at 1.695 eV is attributed to the negatively charged exciton (trion). Polarization-resolved photoluminescence (Supplementary Figs. 25 and 26) was measured under a left-handed circularly polarized (σ_-) laser. The circular helicity is defined as $P = (I_- - I_+)/(I_- + I_+)$, where I_- and I_+ are the intensity of the σ_- and σ_+ components of the photoluminescence signal, respectively. The σ_- and σ_+ components correspond to the exciton transition at K and K′ valleys, respectively, as determined by the valley-selective optical selection rules[40,41]. The circular helicity of the exciton (trion) was 0.28 (0.16) at 77 K, as shown in Fig. 6c, which is comparable to that reported from an exfoliated WSe_2 monolayer flake at the same temperature[42]. The circular helicities of the trion and exciton both drop as a function of increasing temperature (Fig. 6d), which is explained by a higher intervalley scattering rate due to the increased phonon population at high temperatures, consistent with exfoliated WSe_2 monolayers[43]. The observed circular helicity indicates a high level of valley coherence, consistent with a low fraction of IDBs, demonstrating the high quality of the coalesced WSe_2 monolayer[44].

Conclusions

In summary, we demonstrated control of both the nucleation site and unidirectional growth direction of WSe_2 domains grown on *c*-plane sapphire by MOCVD. Steps on the sapphire act as sites for WSe_2 nucleation and impart a preferred domain orientation (0° or 60°) depending on the extent of –OH removal and Se passivation of the sapphire surface. Fully coalesced WSe_2 monolayers with <15% areal coverage of IDBs were obtained across 50-millimetre-diameter substrates. The WSe_2 monolayers exhibited a high level of valley coherence, as assessed by circular helicity measurements, which is consistent with a low fraction of inversion domains.

Online content

Any methods, additional references, Nature Portfolio reporting summaries, source data, extended data, supplementary information, acknowledgements, peer review information; details of author contributions and competing interests; and statements of data and code availability are available at https://doi.org/10.1038/s41565-023-01456-6.

References

1. Acerce, M., Voiry, D. & Chhowalla, M. Metallic 1T phase MoS_2 nanosheets as supercapacitor electrode materials. *Nat. Nanotechnol.* **10**, 313–318 (2015).
2. Late, D. J., Doneux, T. & Bougouma, M. Single-layer $MoSe_2$ based NH_3 gas sensor. *Appl. Phys. Lett.* **105**, 3–7 (2014).
3. Tan, H. et al. Ultrathin 2D photodetectors utilizing chemical vapor deposition grown WS_2 with graphene electrodes. *ACS Nano* **10**, 7866–7873 (2016).
4. Akinwande, D. et al. Graphene and two-dimensional materials for silicon technology. *Nature* **573**, 507–518 (2019).
5. Zhou, H. et al. Large area growth and electrical properties of p-type WSe_2 atomic layers. *Nano Lett.* **15**, 709–713 (2015).
6. Terrones, H., López-Urías, F. & Terrones, M. Novel hetero-layered materials with tunable direct band gaps by sandwiching different metal disulfides and diselenides. *Sci. Rep.* **3**, 1–8 (2013).
7. Yuan, H. et al. Zeeman-type spin splitting controlled by an electric field. *Nat. Phys.* **9**, 563–569 (2013).
8. Xiao, D. et al. Coupled spin and valley physics in monolayers of MoS_2 and other group-VI dichalcogenides. *Phys. Rev. Lett.* **108**, 1–5 (2012).

9. Fang, H. et al. High-performance single layered WSe_2 p-FETs with chemically doped contacts. *Nano Lett.* **12**, 3788–3792 (2012).
10. Radisavljevic, B., Radenovic, A., Brivio, J., Giacometti, V. & Kis, A. Single-layer MoS_2 transistors. *Nat. Nanotechnol.* **6**, 147–150 (2011).
11. Iqbal, M. W. et al. High-mobility and air-stable single-layer WS_2 field-effect transistors sandwiched between chemical vapor deposition-grown hexagonal BN films. *Sci. Rep.* **5**, 10699 (2015).
12. Chuang, H. J. et al. Highmobility WSe_2 p- and n- field-effect transistors contacted by highly doped graphene for low-resistance contacts. *Nano Lett.* **14**, 3594–3601 (2014).
13. Choudhury, T. H., Zhang, X., Al Balushi, Z. Y., Chubarov, M. & Redwing, J. M. Epitaxial growth of two-dimensional layered transition metal dichalcogenides. *Ann. Rev. Mater. Res.* **50**, 155–177 (2020).
14. Mortelmans, W., De Gendt, S., Heyns, M. & Merckling, C. Epitaxy of 2D chalcogenides: aspects and consequences of weak van der Waals coupling. *Appl. Mater. Today* **22**, 100975 (2021).
15. Zhang, X. et al. Diffusion-controlled epitaxy of large area coalesced WSe_2 monolayers on sapphire. *Nano Lett.* **18**, 1049–1056 (2018).
16. Lin, Y. C. et al. Realizing large-scale, electronic-grade two-dimensional semiconductors. *ACS Nano* **12**, 965–975 (2018).
17. Mortelmans, W. et al. Peculiar alignment and strain of 2D WSe_2 grown by van der Waals epitaxy on reconstructed sapphire surfaces. *Nanotechnology* **30**, 465601 (2019).
18. Dong, J., Zhang, L., Dai, X. & Ding, F. The epitaxy of 2D materials growth. *Nat. Commun.* **11**, 5862 (2020).
19. Zhou, W. et al. Intrinsic structural defects in monolayer molybdenum disulfide. *Nano Lett.* **13**, 2615–2622 (2013).
20. Liu, H. et al. Dense network of one-dimensional midgap metallic modes in monolayer $MoSe_2$ and their spatial undulations. *Phys. Rev. Lett.* **113**, 1–5 (2014).
21. Zou, X., Liu, Y. & Yakobson, B. I. Predicting dislocations and grain boundaries in two-dimensional metal-disulfides from the first principles. *Nano Lett.* **13**, 253–258 (2013).
22. Du, L. et al. The effect of twin grain boundary tuned by temperature on the electrical transport properties of monolayer MoS_2. *Crystals* **6**, 1–9 (2016).
23. Zhou, S. et al. Atomically sharp interlayer stacking shifts at anti-phase grain boundaries in overlapping MoS_2 secondary layers. *Nanoscale* **10**, 16692–16702 (2018).
24. Chen, L. et al. Step-edge-guided nucleation and growth of aligned WSe_2 on sapphire via a layer-over-layer growth mode. *ACS Nano* **9**, 8368–8375 (2015).
25. Chubarov, M. et al. Wafer-scale epitaxial growth of unidirectional WS_2 monolayers on sapphire. *ACS Nano* **15**, 2532–2541 (2021).
26. Li, T. et al. Epitaxial growth of wafer-scale molybdenum disulfide semiconductor single crystals on sapphire. *Nat. Nanotechnol.* **16**, 1201–1207 (2021).
27. Hwang, Y. & Shin, N. Hydrogen assisted step-edge nucleation of $MoSe_2$ monolayers on sapphire substrates. *Nanoscale* **11**, 7701–7709 (2019).
28. Suenaga, K. et al. Surface-mediated aligned growth of monolayer MoS_2 and in-plane heterostructures with graphene on sapphire. *ACS Nano* **12**, 10032–10044 (2018).
29. Cohen, A. et al. Tunsten oxide mediated quasi-van der Waals epitaxy of WS_2 on sapphire. *ACS Nano* **17**, 5399–5411 (2023).
30. Chubarov, M., Choudhury, T. H., Zhang, X. & Redwing, J. M. In-plane X-ray diffraction for characterization of monolayer and few-layer transition metal dichalcogenide films. *Nanotechnology* **29**, 055706 (2018).
31. Zheng, P. et al. Universal epitaxy of non-centrosymmetric two-dimensional single-crystal metal dichalcogenides. *Nat. Comm.* **14**, 592 (2023).
32. Tsuda, M. et al. Mechanism of H_2 pre-annealing on the growth of GaN on sapphire by MOVPE. *Appl. Surf. Sci.* **216**, 585–589 (2003).
33. Aljarb, A. et al. Substrate lattice-guided seed formation controls the orientation of 2D transition-metal dichalcogenides. *ACS Nano* **11**, 9215–9222 (2017).
34. Wang, Y. et al. P-type electrical contacts for 2D transition-metal dichalcogenides. *Nature* **610**, 61–66 (2022).
35. Wang, Y. et al. Van der Waals contacts between three-dimensional metals and two-dimensional semiconductors. *Nature* **568**, 70–74 (2019).
36. Garcia, A. et al. Analysis of electron beam damage of exfoliated MoS_2 sheets and quantitative HAADF-STEM imaging. *Ultramicroscopy* **146**, 33–38 (2014).
37. Childres, I. et al. Effect of electron-beam irradiation on graphene field effect devices. *Appl. Phys. Lett.* **97**, 173109 (2010).
38. Reifsnyder Hickey, D. et al. Illuminating invisible grain boundaries in coalesced single-orientation WS2 monolayer films. *Nano Lett.* **21**, 6487–6495 (2021).
39. Huang, P. Y. et al. Grains and grain boundaries in single-layer graphene atomic patchwork quilts. *Nature* **469**, 389–392 (2011).
40. Zeng, H., Dai, J., Yao, W., Xiao, D. & Cui, X. Valley polarization in MoS_2 monolayers by optical pumping. *Nat. Nanotechnol.* **7**, 490–493 (2012).
41. Kim, J. et al. Ultrafast generation of pseudo-magnetic field for valley excitons in WSe_2 monolayers. *Science* **346**, 1205–1208 (2014).
42. Yan, T., Qiao, X., Tan, P. & Zhang, X. Valley depolarization in monolayer WSe_2. *Sci. Rep.* **5**, 15625 (2015).
43. Zhu, B., Zeng, H., Dai, J., Gong, Z. & Cui, X. Anomalously robust valley polarization and valley coherence in bilayer WS_2. *Proc. Natl Acad. Sci. USA* **111**, 11606 (2014).
44. Wang, J. et al. Dual-coupling-guided epitaxial growth of wafer-scale single-crystal WS_2 monolayer on vicinal *a*-plane sapphire. *Nat. Nanotechnol.* **17**, 33–38 (2022).

Methods

MOCVD growth of WSe_2

The WSe_2 films were grown by MOCVD using two systems that are part of the 2D Crystal Consortium MIP facility at Penn State (http://www.mri.psu.edu/2d-crystal-consortium/user-facilities). The first system includes a cold-wall horizontal reactor with inductive heating (MOCVD1) and the second is a multi-module system that includes a cold-wall vertical reactor with resistive heating (MOCVD2). In both systems, tungsten hexacarbonyl ($W(CO)_6$) and hydrogen selenide (H_2Se) were used as the metal and chalcogen precursors, respectively, with hydrogen (H_2) as the carrier gas. $W(CO)_6$ was kept in a stainless-steel bubbler held at a constant temperature (10–20 °C) and pressure (760 torr), and H_2 gas was passed through it to transport the precursor vapour to the reactor. Fifty-millimetre epi-ready *c*-plane sapphire ((0001)α-Al_2O_3) wafers with nominal miscut of 0.2° towards the *m* axis were used as substrates for growth without additional pre-treatment. The reactor pressure was kept constant at 200 torr in MOCVD1 and varied from 50 to 700 torr in MOCVD2. For the growth of WSe_2, a modified three-step process (nucleation, ripening, lateral growth) was employed as illustrated in Supplementary Fig. 3 (refs. 15,25). Additional information on the growth conditions and recipes used for the WSe_2 growth are included in the Supplementary Information.

Layer transfer process

The WSe_2 films were transferred from sapphire for TEM, Raman and photoluminescence spectroscopy. The typical transfer procedure involves coating an as-grown sample with poly(methyl methacrylate) (PMMA) using a spin-coater in two steps: 500 r.p.m. for 15 s followed by 4,500 r.p.m. for 45 s. After curing PMMA at room temperature overnight, the sample edges were mechanically scratched to obtain open sapphire areas that would serve as starting points for the delamination process. The sample was then immersed into 1 M NaOH solution in deionized water and held at 90 °C for 10–15 min. At this point, a few millimetres at the periphery of the 50-mm WSe_2/PMMA films began to detach from the sapphire substrate due to the combined effect of NaOH intercalation at the WSe_2/sapphire interface and sapphire surface etching. The sample was transferred to the top of a deionized water bath (at room temperature), where the delamination front rapidly (that is, within a few tens of seconds) propagated through the entire WSe_2/PMMA film, which peeled off and stayed afloat. This process was mostly aided by hydrophilic character of PMMA and the buoyancy of the WSe_2/PMMA film edges. The assembly was then transferred to a fresh deionized water bath for 10 min for rinsing. This step was then repeated three more times to ensure the complete removal of residual NaOH from the previous step. The assembly was then fished out using a 3-mm-diameter Cu Quantifoil TEM grid or 75-mm SiO_2/Si. After overnight drying at room temperature, the PMMA/WSe_2 film/target substrate assembly was heated at 50 °C for 10 min and at 70 °C for a further 10 min. In the case of TEM, the transfer is performed so that the Quantifoil side touched the WSe_2 film. A fresh drop of PMMA was deposited onto the sample to gently soften the PMMA and improve the contact between the WSe_2 film and the TEM grid. After about 30 min, the sample was placed into an acetone bath for the removal of the PMMA film. The sample was then transferred into an alcohol (methanol or isopropanol) bath to remove the acetone residue. The same procedure was followed for the transfer of the films to the other substrates.

First-principles calculations

All first-principles calculations on structural relaxation were conducted using the Vienna ab initio package[45–47] using the generalized gradient approximation, Perdew–Burke–Ernzerhof[48,49] exchange-correlation functional and the projector augmented wave method pseudopotentials[50,51]. Plane-wave expansions were truncated at an energy cutoff of 400 eV with an electronic loop threshold of 0.1 meV. All structural relaxations were performed using dipole corrections to the total energy and to the electrostatic potential in the out-of-plane direction, until the remaining forces were within 0.01 eV $Å^{-1}$. Gaussian smearing was used with a broadening of 0.05 eV, and van der Waals interactions were treated using the semi-empirical correction of Grimme (zero damping DFT-D3). Brillouin zone samplings were performed within a Γ-centred Monkhorst–Pack scheme on grids with k-point densities equivalent to that of a 20 × 20 × 1 grid for a 1 × 1 *c*-plane Al_2O_3 unit cell. A vacuum layer of 20 Å was inserted normal to the surface to minimize spurious interactions of periodic repetitions.

Material characterization

A Bruker Icon AFM was used to study the surface morphology, domain size, coverage and thickness of the deposited layers. Scanasyst air probe AFM tips with a nominal tip radius of ~2 nm and spring constant of 0.4 N m^{-1} were employed for the measurements, and images were collected using peak-force tapping mode. To measure the thickness of the deposited films, samples were lightly scratched using a blunt tweezer to remove a portion of the weakly bonded WSe_2 film without damaging or scratching the sapphire surface. A Zeiss Merlin electron microscope was used to acquire the scanning electron micrographs. An accelerating voltage of 3 kV and a working distance of 3 mm were used with the in-lens detector to capture the images. Room-temperature Raman and photoluminescence spectroscopy were carried out using a Witec Apyron confocal microscope placed inside a MBraun glovebox to minimize the influence of oxygen (<1 ppm) and moisture (<1 ppm). The laser had an excitation wavelength of 532 nm and the power remained under 4 mW.

WSe_2 FET fabrication and electrical characterization

To fabricate the WSe_2 FETs, monolayer WSe_2 films were first transferred from the sapphire growth substrate to the global backgated Al_2O_3/Pt/TiN/p++-Si substrate using a PMMA-assisted wet transfer process. First the WSe_2 film on the sapphire substrate was spin-coated with PMMA and baked at 150 °C for 2 min to ensure good PMMA–WSe_2 adhesion. The corners of the spin-coated film were scratched using a razor blade and immersed in a 2 M NaOH solution kept at 90 °C. Capillary action caused the NaOH to be preferentially drawn into the substrate/film interface due to the hydrophilic nature of sapphire and the hydrophobic nature of WSe_2 and PMMA, separating the PMMA/WSe_2 film from the sapphire substrate. The separated film was then fished out of the NaOH solution using a clean glass slide and rinsed in three separate water baths for 15 min each before finally being transferred onto the target substrate. Subsequently, the substrate was baked at 50 °C and 70 °C for 10 min each to remove moisture and promote film adhesion, thus ensuring a pristine interface, before the PMMA was removed using acetone immersion overnight and the film was cleaned with IPA.

To define the channel regions on the conformal WSe_2 film, the substrate was spin-coated with PMMA and baked at 180 °C for 90 s. The resist was then exposed via an electron beam (e-beam) and developed using a 1:1 mixture of 4-methyl-2-pentanone (MIBK) and IPA. The bilayer WSe_2 film was subsequently etched using a sulfur hexafluoride (SF_6) reactive ion-etch chemistry at 5 °C for 30 s. Next, the sample was immersed in acetone overnight and cleaned with IPA to thoroughly remove the photoresist.

To define the source and drain contacts, the sample was then spin-coated with MMA followed by A3 PMMA. E-beam lithography was again used to pattern the source and drain contacts. The sample was then developed using a 1:1 mixture of MIBK/IPA for 60 s and pure IPA for 45 s. Next, 40 nm of palladium and 30 nm of gold were deposited using e-beam evaporation. Finally, a lift-off process was performed to remove the evaporated palladium/gold except from the source/drain patterns by immersing the sample in acetone for 30 min followed by IPA rinse for another 10 min.

Electrical characterization of the fabricated devices was performed using a Lake Shore CRX-VF probe station in atmospheric conditions with a Keysight B1500A parameter analyser. Statistical measurements were performed using a semi-automated Formfactor 12000 probe station in atmospheric conditions with a Keysight B1500A parameter analyser.

SHG measurements

SHG measurements were conducted using a 40 fs Ti:sapphire laser (Micra, Coherent) at 800 nm and an 80 MHz repetition rate. The laser beam was passed through a half-wave plate mounted in a rotation stage and was directed into an upright microscope (Olympus) and focused onto a sample surface using a ×100 microscope objective (numerical aperture: NA = 0.9) to a ~1 μm spot. The laser energy at the sample surface was ~0.1 mW. The SHG light was collected in the backscattering configuration using the same objective, and was directed to a monochromator (Spectra Pro 2300i, f = 0.3 m, Acton) that was coupled to the microscope and equipped with a grating with 150 grooves per millimetre and a CCD (charge-coupled device) camera (Pixis 256BR, Princeton Instruments). Before entering the monochromator, the SHG light was passed through a short-pass cutoff filter (650 nm) and a polarizer to filter out the fundamental excitation light at 800 nm and to select the SHG polarization parallel to that of the excitation light. The SHG mapping was conducted by moving a computer controlled motorized XY stage with 0.2 μm steps and acquiring an SHG spectrum at each step with the acquisition time of 0.5 s. To plot the maps, the SHG spectra at each step were integrated from 380 nm to 450 nm.

TEM characterization

DFTEM imaging was performed using a Thermo Fisher Talos F200X microscope operated at 80 kV. Arrays of 5 × 5 DFTEM images were stitched using the GIMP 2 image processing software to make a composite DFTEM map[2]. Briefly, the 25 DFTEM images were loaded into the software and the intensity of each image was adjusted to match with the neighbouring images. At the end, all the Quantifoil regions had a similar intensity and all the free-standing monolayer areas over the Quantifoil holes had a similar intensity. Consequently, the intensity in the bilayer areas would be higher than that of monolayer areas. Finally, the composite image was cropped to a size of 5 μm × 5 μm. Atomic-resolution ADF STEM images were obtained using Thermo Fisher Titan[3] G2 60–300 microscope operated at 80 kV. Other acquisition parameters used were a 30 mrad semiconvergence angle, 50 pA screen current and 42–244 mrad ADF detector collection angle range. A two-pixel Gaussian blur was applied to the ADF STEM image shown in Supplementary Fig. 23d.

Cross-sectional TEM samples were prepared using a FEI Helios 660 focused ion beam system. A thick protective amorphous carbon layer was deposited over the region of interest, then Ga+ ions (30 kV then stepped down to 1 kV to avoid ion beam damage to the sample surface) were used in the focused ion beam to make the e-beam transparent samples. High-resolution STEM was performed at 300 kV on a dual spherical aberration-corrected FEI Titan G2 60–300 S/TEM. All the STEM images were collected by using a HAADF detector with a collection angle of 50–100 mrad.

Low-temperature and polarization-dependent photoluminescence measurements

The WSe_2 transferred on Si was cooled down to 77 K using liquid nitrogen in a Janis ST-500 cryostat before photoluminescence measurements were performed on a home-made optical spectroscope. The incident 532 nm continuous wave laser was passed through a linear polarizer and a quarter-wave plate to generate the left-handed circular polarized light that was focused on the sample using a ×50 objective with a NA of 0.4. The circularly polarized photoluminescence signal was collected by the same quarter-wave plate and another linear polarizer, which was rotated to select the polarization of the photoluminescence signals. The laser power used was around 0.2 mW.

Data availability

Additional data relevant to the conclusions of this study are available in the Supplementary Information. Growth and characterization data associated with the samples produced in this study are available via ScholarSphere[52]. This includes substrate preparation and recipe data for samples grown by MOCVD in the 2DCC-MIP facility and standard characterization data including AFM images, room-temperature Raman/photoluminescence spectra and field-emission scanning electron microscopy images of the samples. Videos associated with the DFT results are included as Supplementary Videos 1–8 and are available via figshare at https://doi.org/10.6084/m9.figshare.23274647 (ref. 53). Additional datasets related to DFT, SHG, TEM, FET and low-temperature photoluminescence are available from the corresponding author upon request.

References

45. Kresse, G. & Furthmüller, J. Efficiency of ab-initio total energy calculations for metals and semiconductors using a plane-wave basis set. *Comput. Mater. Sci.* **6**, 15–50 (1996).
46. Kresse, G. & Furthmüller, J. Efficient iterative schemes for ab initio total-energy calculations using a plane-wave basis set. *Phys. Rev. B* **54**, 11169–11186 (1996).
47. Kresse, G. & Hafner, J. Ab initio molecular dynamics for liquid metals. *Phys. Rev. B* **47**, 558–561 (1993).
48. Perdew, J. P., Burke, K. & Ernzerhof, M. Generalized gradient approximation made simple. *Phys. Rev. Lett.* **77**, 3865–3868 (1996).
49. Perdew, J. P., Burke, K. & Ernzerhof, M. Generalized gradient approximation made simple. *Phys. Rev. Lett.* **77**, 3865–3868 (1996); erratum **78**, 1396 (1997).
50. Kresse, G. & Joubert, D. From ultrasoft pseudopotentials to the projector augmented-wave method. *Phys. Rev. B* **59**, 1758–1775 (1999).
51. Kresse, G. & Hafner, J. Norm-conserving and ultrasoft pseudopotentials for first-row and transition elements. *J. Phys. Condens. Matter* **6**, 8245–8825 (1994).
52. Redwing, J. et al. WSe_2 on c-plane sapphire with preferred orientation grown by MOCVD. *ScholarSphere* https://doi.org/10.26207/f7b1-fs46 (2023).
53. Nayir, N. & van Duin, A. C. T. Movies showing the nucleation of WSe_2 on Al_2O_3 with mixed (Se/O) and single (Se) steps. figshare https://doi.org/10.6084/m9.figshare.23274647 (2023).

Acknowledgements

The work was financially supported by the National Science Foundation (NSF) through the Pennsylvania State University 2D Crystal Consortium–Materials Innovation Platform (2DCC-MIP) under NSF cooperative agreement numbers DMR-1539916 and DMR-2039351. S.B. and N.A. acknowledge support provided by NSF Career grant number DMR-1654107. T.V.M. and J.M.R. acknowledge support from the Defense Technical Information Center under award number FA9550-21-1-0460. N.T. acknowledges support from the NSF Graduate Research Fellowship Program under grant number DGE1255832. K.Z. and S.H. acknowledge support from NSF under grant numbers ECCS-1943895 and ECCS-2246564 and Air Force Office of Scientific Research under grant number FA9550-22-1-0408. SHG measurements were supported by the Center for Nanophase Materials Sciences (CNMS), which is a US Department of Energy Office of Science User Facility at Oak Ridge National Laboratory.

Author contributions

H.Z. and T.H.C. carried out MOCVD growth, AFM, field-emission scanning electron microscopy and in-plane XRD characterization

and data analysis with assistance from K.Y., T.V.M.K., N.T., R.A.M. and S.M.D. N.N., V.H.C. and A.C.T.v.D. carried out DFT calculations. A.B. and B.H. performed in-plane XRD, layer transfer and Raman/photoluminescence characterizations. K.Z. and S.H. performed low-temperature and polarization-resolved photoluminescence measurements. A.A.P. performed SHG characterization. S.B., N.A. and K.W. performed transmission electron microscopy characterizations. A.O. and S.D. fabricated and tested backgated FETs. H.Z., N.N., T.H.C. and J.M.R. co-wrote the manuscript with input from all authors. All authors contributed to the discussions.

Competing interests

The authors declare no competing interests.

Additional information

Supplementary information The online version contains supplementary material available at https://doi.org/10.1038/s41565-023-01456-6.

Correspondence and requests for materials should be addressed to Joan M. Redwing.

Peer review information *Nature Nanotechnology* thanks Wouter Mortelmans and the other, anonymous, reviewer(s) for their contribution to the peer review of this work.